Earth and Planetary Science Letters 341-344 (2012) 243–254

Contents lists available at SciVerse ScienceDirect

Earth and Planetary Science Letters

journal homepage: www.elsevier.com/locate/epsl

The evolution of pCO_2, ice volume and climate during the middle Miocene

Gavin L. Foster [a,*], Caroline H. Lear [b], James W.B. Rae [c]

[a] Ocean and Earth Science, National Oceanography Centre Southampton, University of Southampton Waterfront Campus, Southampton SO14 3ZH, UK
[b] School of Earth and Ocean Sciences, Cardiff University, Main Building, Park Place, Cardiff CF10 3AT, UK
[c] Bristol Isotope Group, Department of Earth Sciences, University of Bristol, Wills Memorial Building, Queens Road, Bristol BS8 1RJ, UK

ARTICLE INFO

Article history:
Received 16 December 2011
Received in revised form
10 May 2012
Accepted 4 June 2012
Editor: G. Henderson
Available online 20 July 2012

Keywords:
boron isotopes
middle Miocene
pCO_2
climate change

ABSTRACT

The middle Miocene Climatic Optimum (17–15 Ma; MCO) is a period of global warmth and relatively high CO_2 and is thought to be associated with a significant retreat of the Antarctic Ice Sheet (AIS). We present here a new planktic foraminiferal $\delta^{11}B$ record from 16.6 to 11.8 Ma from two deep ocean sites currently in equilibrium with the atmosphere with respect to CO_2. These new data demonstrate that the evolution of global climate during the middle Miocene (as reflected by changes in the cyrosphere) was well correlated to variations in the concentration of atmospheric CO_2. What is more, within our sampling resolution (~1 sample per 300 kyr) there is no evidence of hysteresis in the response of ice volume to CO_2 forcing during the middle Miocene, contrary to what is understood about the Antarctic Ice Sheet from ice sheet modelling studies. In agreement with previous data, we show that absolute levels of CO_2 during the MCO were relatively modest (350–400 ppm) and levels either side of the MCO are similar or lower than the pre-industrial (200–260 ppm). These new data imply the presence of either a very dynamic AIS at relatively low CO_2 during the middle Miocene or the advance and retreat of significant northern hemisphere ice. Recent drilling on the Antarctic margin and shore based studies indicate significant retreat and advance beyond the modern limits of the AIS did occur during the middle Miocene, but the complete loss of the AIS was unlikely. Consequently, it seems that ice volume and climate variations during the middle Miocene probably involved a more dynamic AIS than the modern but also some component of land-based ice in the northern hemisphere.

1. Introduction

Over at least the last 550 thousand years Earth's climate, global sea level, and the CO_2 content of the atmosphere have been tightly coupled (Rohling et al., 2009). However, the nature of this relationship in the future in response to anthropogenic climate change is hard to predict (Rahmstorf et al., 2007) due to questions regarding the behaviour of the large continental scale ice sheets of Greenland and Antarctica in a rapidly warming climate (Alley et al., 2005). Observations of continental ice sheet stability in the past, when the Earth's climate was significantly warmer than today, may not represent the immediate future due to hysteresis in ice sheet behaviour (Pollard and DeConto, 2005), but do provide a valuable test-bed of our understanding of ice sheet growth and decay (Pollard and DeConto, 2005).

The Cenozoic era saw a fundamental transition in the Earth's climate state from the greenhouse climate of the Cretaceous to our modern icehouse, characterised by continental ice on both poles (Zachos et al., 2001). Large, continental scale ice sheets first formed on Antarctica at the Eocene–Oligocene boundary (33.7 Ma; Coxall et al., 2005), while the northern hemisphere is thought to have remained largely ice free until the Late Pliocene (~3 Ma; DeConto et al., 2008; Zachos et al., 2001; Mudelsee and Raymo, 2005). The modern Antarctic Ice Sheet (AIS) is made up of two parts, the large, sluggish, land-based Eastern AIS and the smaller, more dynamic, largely marine-based Western AIS. Ice sheet modelling indicates that, once formed, the land-based AIS is very difficult to melt (Pollard and DeConto, 2005). This hysteresis effect arises because the bright surface of the ice cap maintains a cold, elevated interior that resists melting during a global warming event. Such modelling also indicates that CO_2 levels must rise to significantly higher values in order to melt the EAIS than are required to form it in the first place (~1000 ppm vs. 750–840 ppm; Pollard and DeConto, 2005). In contrast, no significant hysteresis is thought to characterise the marine-based AIS (Pollard and DeConto, 2009) or is documented in records of the northern hemisphere ice sheets response to climate forcing (Rohling et al., 2009).

Throughout the Oligocene and Miocene there is a growing body of evidence for orbitally paced and relatively large ($\pm$ >20 m) changes in sea level and ice volume, often attributed to growth/decay of the land-based Antarctic Ice Sheet (e.g. Pekar

* Corresponding author.
E-mail address: Gavin.Foster@noc.soton.ac.uk (G.L. Foster).

0012-821X/$ - see front matter © 2012 Elsevier B.V. All rights reserved.
http://dx.doi.org/10.1016/j.epsl.2012.06.007

and DeConto, 2006; Holbourn et al., 2007; Shevenell et al., 2008; Kominz et al., 2008; Liebrand et al., 2011; Passchier et al., 2011). The middle Miocene Climatic Optimum (MCO; 17–15 Ma) is one such time period where the Antarctic Ice Sheet may have reduced in size, with some studies suggesting a decrease to around 10–25% of its modern volume (De Boer et al., 2010). This period is however characterised by rather limited global warmth (+2–4 °C compared to preindustrial; You et al., 2009) with reconstructions of CO_2 showing either relatively stable levels with concentrations similar to the pre-industrial (200–300 ppm; Pagani et al., 1999) or, if elevated at all (350–450 ppm; Kürschner et al., 2008), well below the modelled threshold values required to melt the land-based AIS (e.g. ~1000 ppm; Pollard and DeConto, 2005). Therefore, a puzzling aspect of the climate evolution of the MCO is why the observed rapid and orbitally paced variations in sea level and ice volume (e.g. Holbourn et al., 2007) take place without appearing to show significant hysteresis. This discrepancy between geological observations and ice sheet modelling implies that either our understanding of how the continental ice sheets grow and decay is at fault or our reconstructions of the middle Miocene CO_2 and climate are in error. Here we present a new multi-site boron isotope-based reconstruction of surface water palaeo-pH and use this to quantify the evolution of atmospheric CO_2 during this time period (e.g. Hönisch and Hemming, 2005; Foster, 2008). This new pCO_2 reconstruction allows, for the first time, a direct investigation of the relationship between pCO_2 and the cyrosphere of the middle Miocene.

2. Materials and methods

2.1. Sample locations and site details

We examine Miocene aged sediments from two open ocean Sites: ODP 761 from the Wombat Plateau (16°44.23′S, 115°32.10′E and water depth of 2179 m) and ODP 926 from the Ceara Rise (3°43.148′N, 42°54.507′W and water depth of 3598 m). Both Sites are currently located in regions where surface water is close to equilibrium with the atmosphere with respect to CO_2 (Fig. 1; Takahashi et al., 2009).

The foraminifera sampled from ODP Hole 761B were taken from between 35 and 50 m below sea floor (mbsf), which is an unusually shallow burial depth for a middle Miocene sequence. In comparison, foraminifera from ODP Site 926 were sampled from between 238 and 291 mbsf. These contrasting burial depths suggest that foraminifera from ODP Site 926 would in all likelihood be subject to more micro-crystalline recrystallisation than ODP Site 761 (Schrag, 1999). We also note that the intermediate water depth of ODP Site 761 would limit the degree of seafloor dissolution of planktic foraminiferal tests, which has been shown to affect the trace metal and boron isotope composition of some species (Brown and Elderfield, 1996; Hönisch and Hemming, 2004; Seki et al., 2010). Comparison of the two sites may thus allow us to assess potential diagenetic effects on our $\delta^{11}B$ data.

2.2. Analytical methodology

Between 100 and 150 tests of *Globigerinoides sacculifer* without sac-like final chamber (also known as *G. trilobus* in the Miocene) were picked from the 300–355 μm size fraction from ODP Sites 761 and 926 (Fig. S1). From one sample depth at ODP Site 761 we also picked 10–15 *Cibicidoides mundulus* and *Cibicidoides wuellerstorfi* from the >250 μm fraction. All samples were crushed and cleaned following the established oxidative cleaning method (Barker et al., 2003; Yu et al., 2007). Samples were dissolved in 0.075–0.1 M HNO_3, centrifuged shortly after dissolution to remove any insoluble residue, and transferred to screw top 5 ml Teflon vials for storage before analysis.

A small aliquot (< 10%) of each sample for boron isotope analysis was taken and analysed for trace element composition using a ThermoFisher Scientific Element 2 at the University of Bristol following the methodology outlined in Foster (2008). This tandem trace element analysis allowed an assessment of cleaning efficiency and provided the Mg/Ca ratios used to estimate ocean temperature. The long term reproducibility of Mg/Ca is ~1.5% at 95% confidence based on repeat measurements of three consistency standards over the last 2 yr at Bristol. Sea surface temperatures were calculated using the generic Mg/Ca temperature equation (Anand and Elderfield, 2003), *G. sacculifer* Mg/Ca and a seawater Mg/Ca ratio (Mg/Ca_{sw})=3.43 mol/mol from fluid inclusions (Horita et al., 2002). The deep water temperatures required to estimate deep water pH (see below), were calculated using the same Mg/Ca_{sw} and the Mg/Ca of *C. mundulus* and Eq. (2) of Lear et al. (2002; Table S1).

Boron was separated from our dissolved samples using amberlite IRA-743 boron-specific anion exchange resin following previously established methods (Foster, 2008). The boron isotopic composition was determined using a sample-standard bracketing routine on a ThermoFisher Scientific Neptune multicollector inductively coupled plasma mass spectrometer (MC-ICPMS) at the University of Bristol (Foster, 2008). The full sample data set is shown in Table S1 and external precision is sample size dependent and varies from ±0.23‰ to 0.41‰ (calculated as described in Rae et al., 2011).

2.3. Boron isotopes and palaeo-pH

Boron exists predominantly as two species in aqueous solutions at typical ocean pH: boric acid [$B(OH)_3$] and borate ion [$B(OH)_4^-$], and their relative abundance is dependent on pH (Fig. 2). There are two isotopes of boron, ^{10}B and ^{11}B, with natural abundances of ~20% and ~80%, respectively. Isotope variations

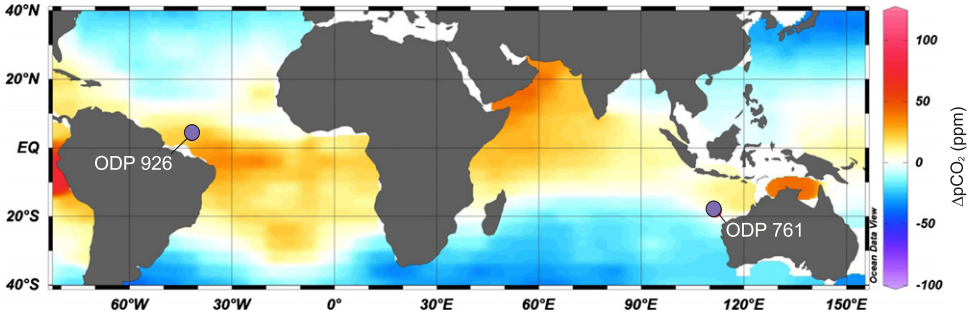

Fig. 1. Mean annual air–sea disequilibria with respect to pCO_2. Purple dots indicate the location of the sites used in this study. ODP 761 (16°44.23′S, 115°32.10′E) is from a water depth of 2179 m and ODP 926 (3°43.148′N, 42°54.507′W) is from 3598 m. The modern extent of disequilibria at both sites is <25 ppm. Data from Takahashi et al. (2009). (For interpretation of the references to colour in this figure legend, the reader is referred to the web version of this article.)

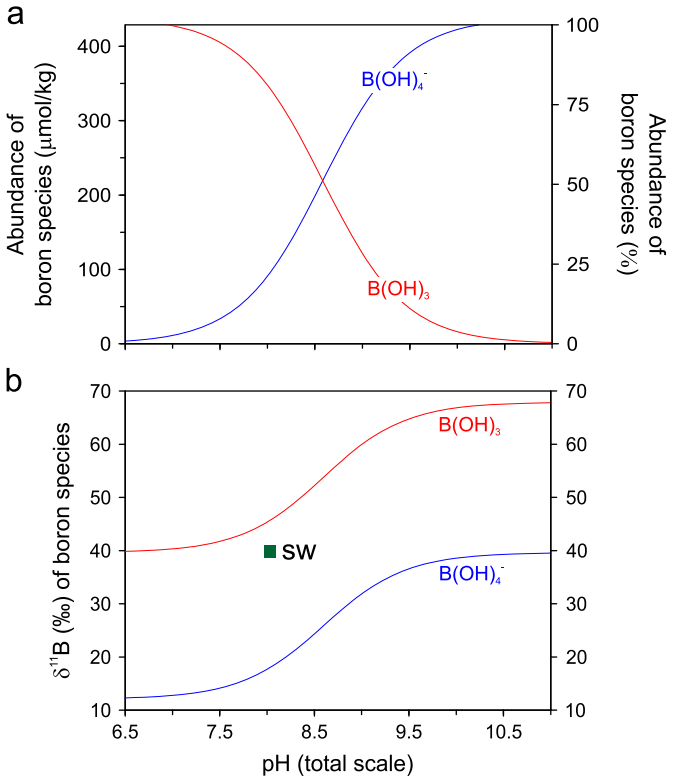

Fig. 2. Concentration (a) and isotopic composition (b) of borate ion [$B(OH)_4^-$] and boric acid [$B(OH)_3$] with seawater pH (total scale). Graphs are plotted for typical surface ocean conditions (T=25 °C, S=35 psu) with $\delta^{11}B$ seawater=39.61‰ (green square; Foster et al., 2010) and total boron of 432.6 μmol/kg (Lee et al., 2010). (For interpretation of the references to colour in this figure legend, the reader is referred to the web version of this article.)

are described in delta notation as follows:

$$\delta^{11}B = \left[\left(\frac{^{11}B/^{10}B_{sample}}{^{11}B/^{10}B_{NIST951}}\right)-1\right]\times 1000 \quad (1)$$

where $^{11}B/^{10}B_{NIST951}$ is the $^{11}B/^{10}B$ ratio of NIST SRM 951 boric acid standard ($^{11}B/^{10}B$=4.04367; Catanzaro et al., 1970).

Due to structural differences between the two aqueous boron species there is a pronounced isotopic fractionation between them in seawater, with $B(OH)_3$ being enriched in ^{11}B compared to $B(OH)_4^-$. Since the concentration of each species is pH dependent, in order to maintain a constant $\delta^{11}B$ of seawater, the isotopic composition of each species also varies according to pH (Fig. 2). The isotopic composition of $B(OH)_4^-$ is therefore related to pH as follows:

$$pH = pK_B^* - \log\left(-\frac{\delta^{11}B_{SW}-\delta^{11}B_{B(OH)_4^-}}{\delta^{11}B_{SW}-\alpha_B\,\delta^{11}B_{B(OH)_4^-}-((\alpha_B-1)1000)}\right) \quad (2)$$

where pK_B^* is the $-1\log_{10}$ of the stoichiometric equilibrium constant for boric acid (Dickson, 1990) at the *in situ* temperature, salinity and pressure, $\delta^{11}B_{sw}$ is the isotopic composition of seawater (39.61‰; Foster et al., 2010) and $\delta^{11}B_{B(OH)_4^-}$ is isotopic composition of borate ion. α_B is the isotopic fractionation between the two aqueous species of boron in seawater and has recently been determined as 1.0272 ± 0.0006‰ (Klochko et al., 2006).

On the basis of isotopic measurements of marine carbonates, (Hemming et al., 1992) suggested that the borate ion species is preferentially incorporated into marine carbonate. However, NMR studies (Klochko et al., 2009) have shown that some trigonally coordinated boron is also present in $CaCO_3$, which has been used by some to argue that boric acid may also be incorporated into $CaCO_3$ (Klochko et al., 2009; Rollion-Bard et al., 2011). Recent isotopic measurements of benthic foraminifera by MC-ICPMS however confirm that only very minor amounts of boric acid can possibly be incorporated in foraminifera (< 1%; Rae et al., 2011). Consequently, for epifaunal benthic foraminifera measured by MC-ICPMS $\delta^{11}B_{foram} = \delta^{11}B_{B(OH)_4^-}$ and Eq. (2) can be used to calculate pH from $\delta^{11}B_{foram}$ (Rae et al., 2011).

For the planktic foraminifera *G. sacculifer* used here, it has been shown using MC-ICPMS (Foster, 2008) and negative ion thermal ionisation mass spectrometry (NTIMS; Sanyal et al., 2001), that $\delta^{11}B$ has a strong pH dependency but $\delta^{11}B_{foram} \neq \delta^{11}B_{B(OH)_4^-}$. Fig. 3 shows that $\delta^{11}B$ of cultured *G. sacculifer* ($\delta^{11}B_{sac}$) exhibits around 90% of the pH sensitivity of the $\delta^{11}B$ of $B(OH)_4^-$ and the following relationship is evident:

$$\delta^{11}B_{B(OH)_4^-} = (\delta^{11}B_{sac} - 7.15)/0.88 \quad (3)$$

Part of this difference compared to $\delta^{11}B_{B(OH)_4^-}$ is likely due to the effect of photosynthetic symbionts modifying the micro-environment around the growing foraminifera (Zeebe et al., 2003; Hönisch et al., 2003). However, a comparison to the core top MC-ICPMS data for *G. sacculifer* (500–600 μm; Foster, 2008) also implies a large portion is due to analytical bias (see discussion in Rae et al., 2011; Fig. 3). Nonetheless, it is likely that relative changes are accurately reconstructed by NTIMS (Sanyal et al., 1995; Hönisch and Hemming, 2005; Ni et al., 2010; Rae et al., 2011) so the gradient (the pH sensitivity of $\delta^{11}B_{sac}$) described by the culture data is likely applicable to MC-ICPMS analyses even if the intercept is not (Fig. 3). The $\delta^{11}B$ of *G. sacculifer* is known to vary with test size (Hönisch and Hemming, 2004; Ni et al., 2007) and there is an offset of ~1‰ between *G. sacculifer* (500–600 μm) and *G. sacculifer* (300–355 μm; Seki et al., 2010). We therefore modify the intercept until it passes through the core top value for *G. sacculifer* (300–355 μm) from ODP 999A of Seki et al. (2010). We can thus use the following to calculate the appropriate $\delta^{11}B_{B(OH)_4^-}$ for *G. sacculifer* (300–355 μm; $\delta^{11}B_{sac}$):

$$\delta^{11}B_{B(OH)_4^-} = (\delta^{11}B_{sac} - 1.85)/0.88 \quad (4)$$

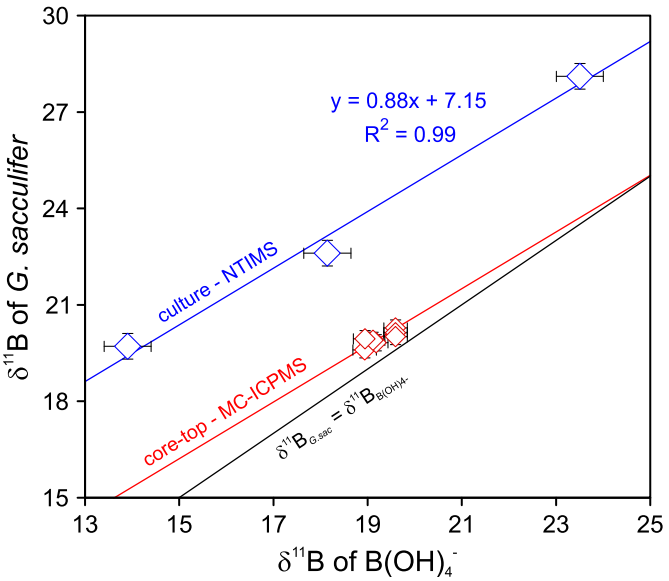

Fig. 3. Relationship between $\delta^{11}B$ of *G. sacculifer* and the $\delta^{11}B$ of borate ion [$B(OH)_4^-$] in seawater. The culture data of Sanyal et al. (2001) defines the relationship between $\delta^{11}B$ of $B(OH)_4^-$ in seawater and the $\delta^{11}B$ of *G. sacculifer*. Due largely to analytical offsets (see Foster, 2008; Rae et al., 2011; Ni et al., 2010) the core-top data measured by MC-ICPMS (from Foster, 2008) are consistently lighter but define a similar relationship. The intercept of the relationship defined by the culture data is thus refitted through the core-top data to define the appropriate relationship for *G. sacculifer* measured by MC-ICPMS (see text for further details).

The $\delta^{11}B_{B(OH)_4^-}$ calculated from the measured $\delta^{11}B_{sac}$ can then be inserted into Eq. (2) to calculate pH. Since *G. sacculifer* is a predominantly a mixed layer dweller we assume here the calculated pH using this equation is that of surface water.

The stoichiometric dissociation constant of boric acid (K_B^*) is temperature, salinity and pressure dependent. These variables do not have a large impact on the calculated pH (e.g. ± 1 °C$= \pm 0.01$ pH units; ± 1 psu$= \pm 0.006$ pH units), uncertainties in which, for a given value of $\delta^{11}B_{sw}$, are driven largely by the analytical uncertainties in our $\delta^{11}B_{foram}$ determination (± 0.2‰$= \pm 0.02$ pH units). Deep water and surface water temperatures are determined as described above and salinity is assumed to be 35 psu throughout. Pressure is assumed to be 0 for *G. sacculifer* and the palaeo-depth of ODP Site 761 (189 bar; Holbourn et al., 2004) is used for *C. mundulus* and *C. wuellerstorfi*.

2.4. The $\delta^{11}B$ of seawater during the middle Miocene

Although the modern $\delta^{11}B_{sw}$ is well constrained at 39.61‰ (Foster et al., 2010), geochemical modelling suggests significant variations in $\delta^{11}B_{sw}$ are likely to have occurred through the Cenozoic (Lemarchand et al., 2002; Simon et al., 2006). The residence time for boron is however sufficiently long (~10–20 Ma) that its isotopic composition is unlikely to have changed significantly during the 4 million year period we examine here (Lemarchand et al., 2002). These published geochemical models only semi-quantitatively constrain the evolution of $\delta^{11}B_{sw}$ and there are only two studies that have so far attempted to empirically reconstruct $\delta^{11}B_{sw}$ during the Cenozoic and they reconstruct quite different values (Pearson and Palmer, 2000; Paris et al., 2010). There is therefore a pressing need for more accurate estimates of $\delta^{11}B_{sw}$ in the past.

Here we propose two methods to estimate $\delta^{11}B_{sw}$:

(1) Assume the modern surface to deep pH gradient at the Wombat Plateau (0.254 pH units; Key et al., 2004) is applicable to the middle Miocene. Given a known pH difference between benthic and planktic foraminifera, and because of the non-linear relationship between pH and $\delta^{11}B$ (Fig. 2), we can tune the $\delta^{11}B_{sw}$ until our measured $\delta^{11}B$ values for *G. sacculifer* (planktic), *C. mundulus* and *C. wuellerstorfi* (benthic) give a pH difference of 0.254 pH units.

(2) pH is determined by the ratio of total alkalinity (ALK) to total dissolved inorganic carbon (DIC) and the depth profile of pH at any one place in the ocean depends largely on the processes that operate to modify this ratio. Most significant is the operation of the organic carbon pump, which removes DIC from the surface ocean through photosynthesis and adds DIC to the deep sea as a consequence of the oxidation of sinking organic carbon particulates. Changes in the strength of the organic pump will thus change the pH gradient from surface to deep (the main limitation of the approach (1) above). Like pH, the carbon isotopic composition of DIC is also largely controlled by the operation of the organic carbon pump. This is because biological utilisation of isotopically "light" carbon in the surface ocean drives the $\delta^{13}C_{DIC}$ towards heavier values, and the oxidation of this organic carbon at depth drives $\delta^{13}C_{DIC}$ towards lighter values. As with pH, changes in the strength of the organic carbon pump changes the surface to deep gradient in $\delta^{13}C_{DIC}$. Because these two parameters (pH gradient and $\delta^{13}C_{DIC}$ gradient) are largely controlled by the same phenomenon (organic carbon pump) they are well correlated in the oceans and the relationship can be parameterised quite simply (Fig. 4). Crucially, if the strength of the organic carbon pump differed in the past then

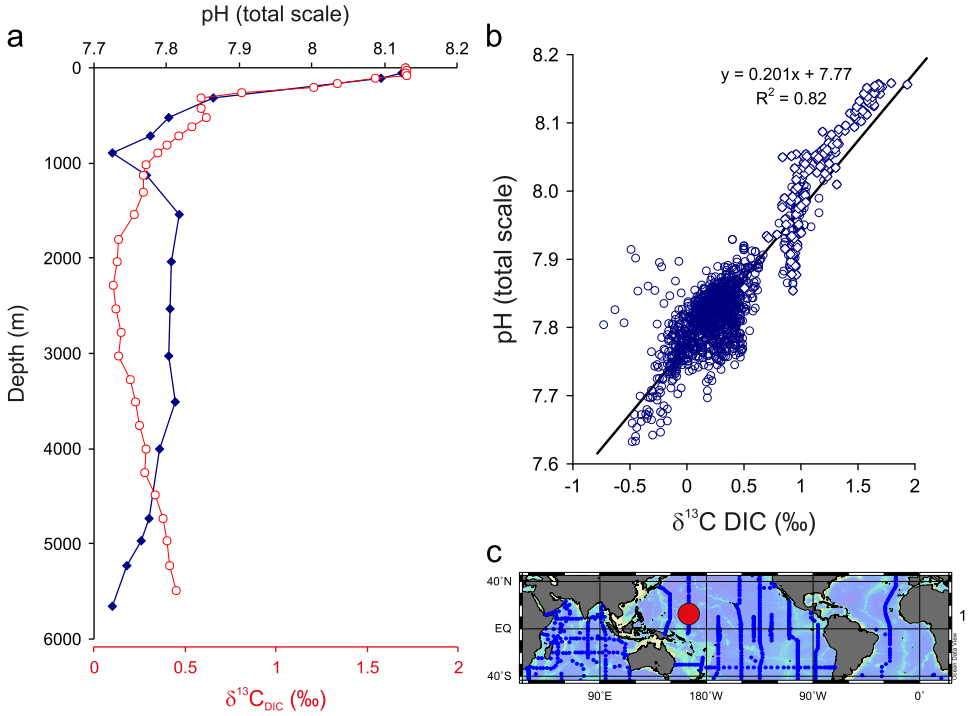

Fig. 4. pH and $\delta^{13}C_{DIC}$ relationships with depth in the modern ocean. (a) Depth vs. pH and $\delta^{13}C_{DIC}$ at a site from the equatorial Pacific (red dot in c). (b) Cross plot of pH vs. $\delta^{13}C_{DIC}$ for all the sites shown in (c; open circles). Because of anthropogenic acidification and the Seuss effect only data from >1500 m are plotted in (b). Also shown in (b) are the data from a transect in the North Atlantic (from 0 to 5000 m) where the effects of anthropogenic perturbation on both parameters have been corrected (blue diamonds; Olsen and Ninneman, 2010). The linear fit through both datasets can be described as: pH$=0.201*\delta^{13}C_{DIC} +7.77$ ($R^2=0.82$). We note that because pH is a logarithmic function we should not expect a linear fit, however for simplicity we adopt this approximation here. (For interpretation of the references to colour in this figure legend, the reader is referred to the web version of this article.)

both the surface to deep pH and $\delta^{13}C_{DIC}$ gradients will change in a predictable, and related, way (Fig. 4). For example, if the strength of the organic carbon pump increased, increasing the surface to deep $\delta^{13}C_{DIC}$ gradient from 1‰ to 1.5‰, the relationship in Fig. 4b indicates the surface to deep pH gradient would increase from 0.2 pH units to 0.3 pH units. Because the $\delta^{13}C_{DIC}$ can be reconstructed from the $\delta^{13}C$ of foraminifera (after accounting for vital effects), by measuring the $\delta^{13}C$ of two (or more) foraminifera that inhabit different locations or depths in the oceans, it is possible to reconstruct the $\delta^{13}C_{DIC}$ difference between them (e.g. $\Delta\delta^{13}C_{DICsurface\text{-}deep}$) and hence calculate the pH difference between them ($\Delta pH_{surface\text{-}deep}$) assuming the relationship shown in Fig. 4b remains constant through time. The main controls on the slope of the pH vs. $\delta^{13}C_{DIC}$ gradient are: (i) the strength of the alkalinity pump which changes ALK/DIC (and hence pH) with a ratio of roughly 2/1 but does not significantly influence $\delta^{13}C_{DIC}$ (since the $\delta^{13}C_{DIC} \approx \delta^{13}C$ of marine $CaCO_3$); (ii) the extent and temperature of air–sea gas exchange at high latitudes which modifies CO_2 solubility and $\delta^{13}C_{DIC}$ of water masses ventilated in these regions (e.g. Lynch-Stieglitz et al., 1995); and (iii) the concentration of CO_2 which influences the magnitude of the carbon isotopic fractionation between phytoplankton and $[CO_2]_{aq}$ and hence the magnitude of the $\delta^{13}C_{DIC}$ gradient that develops (e.g. Freeman and Hayes, 1992). Future studies will more thoroughly assess the limitations of this method and the influences of these and other factors in more detail. In the mean time here, to minimise the influence of these uncertainties, we have chosen to use benthic and planktic data from the relatively stable period at 12.72 Ma, which is outside of the Monterey $\delta^{13}C$ excursion and associated variations in the CCD (e.g. Lyle, 2003), and is a time when reconstructions of the oceanic $\delta^{13}C$ depth profile (see Woodruff and Savin (1991); their Fig. 18) appear most similar to the modern. Antarctic frontal systems also appear to have reached near to present configuration by the Middle to Late Miocene (Cooke et al., 2002), possibly indicating similar air–sea gas exchange processes operating in the region as today. Furthermore, alkenone-based studies of $\delta^{13}C$ fractionation between organic matter and $[CO_2]_{aq}$ show only minor differences relative to today (Pagani et al., 1999). Together these observations provide strong support for our use of the modern slope of $\delta^{13}C_{DIC}$ vs. pH to estimate seawater $\delta^{11}B$.

2.5. Second carbonate system parameter

Like pH, $[CO_2]_{aq}$ at a given oceanic location is also largely determined by the ALK to DIC ratio. In order to estimate $[CO_2]_{aq}$ and hence pCO_2 from pH, one other carbonate system variable is needed, though it is important to note that, given this close relationship between pH and $[CO_2]_{aq}$ in a given parcel of water, reconstructed CO_2 variations will be chiefly driven by $\delta^{11}B$-derived pH. Due to the relationships of the different carbonate system parameters in the oceans, estimates of the "master variables" ALK or DIC, rather than $[CO_3^{=}]$ for instance, are considered the best 2nd carbonate system parameter with which to calculate pCO_2 from pH. To estimate surface ALK we use a simple model describing the deep (3100 m), intermediate (1890 m) and surface ocean (0 m). We constrain this model using a number of parameters/assumptions: (i) the depth of the CCD, which is relatively well known for the Miocene (Sime et al., 2007). However, it has been shown (Lyle, 2003; Lear et al., 2010) that over the course of the MMCT there are short term changes in the $[CO_3^{=}]$ of the deep ocean, and consequently the CCD, that are not picked up by the lower resolution reconstructions (Sime et al., 2007). To avoid uncertainties in these CCD reconstructions we estimate surface alkalinity at 12.72 Ma, after the MMCT, and use the same ALK for our entire record. Variations in the depth of the CCD (or variations in the depth of the CCD relative to the saturation horizon) by ± 500 m result in variations of ± 100 μmol/kg in our estimate of deep water alkalinity. (ii) The pH of the intermediate depth ocean which is determined by the $\delta^{11}B$ of benthic foraminifera from ODP 761 (which is dependent on $\delta^{11}B_{sw}$). (iii) The pH and temperature difference between the intermediate and deep ocean, which is assumed to be zero based on modern observations. For instance the typical pH and temperature gradient from 2000 m to 3000 m is <0.05 pH units and <2 °C. (iv) The magnitude of the surface to deep water alkalinity gradient is assumed to be the same as the modern gradient at the Wombat Plateau (-100 μmol/mol). This gradient varies in the modern ocean from -200 to $+100$ μmol/kg.

2.6. Carbonate system calculations

Here and throughout we use the various constants for the carbonate system calculations as recommended by Dickson et al. (2007) with a modern seawater boron concentration (432.6 μmol/kg; Lee et al., 2010). We also account for the effect of changing [Mg] and [Ca] of seawater (reconstructed from fluid inclusions; Horita et al., 2002) on the carbonic acid dissociation constants K_1 and K_2 and the solubility product of calcite (Tyrrell and Zeebe, 2004). We do not account for the influence of changing seawater composition on pK_B as these effects are poorly known and likely to be minor for the middle Miocene (equivalent to <30 ppm CO_2; Hershey et al., 1986).

3. Results and discussion

3.1. $\delta^{11}B$ of *G. sacculifer* from the middle Miocene

The boron isotope data for *G. sacculifer* from our two Sites are in good agreement and show lower $\delta^{11}B$ values (15.0 ± 0.4‰ to 15.8 ± 0.3‰) during the MCO, with higher values (16.0 ± 0.3‰ to 17.1 ± 0.2‰) either side of this warm period, largely sympathetic with the benthic foraminiferal $\delta^{18}O$ record for this time period (Fig. 5). The $\delta^{11}B$ of foraminifera such as *G. sacculifer* ($\delta^{11}B_{sac}$) has a positive relationship with pH (Fig. 2), and thus a negative relationship with $[CO_2]_{aq}$. Therefore, the $\delta^{11}B$ of *G. sacculifer* may reflect both the atmospheric concentration of CO_2 (pCO_2) and local $[CO_2]_{aq}$ changes due to hydrography (e.g. upwelling). Surface water above both sites is currently close to equilibrium with the atmosphere with respect to CO_2 (Fig. 1), and given the similarity of the $\delta^{11}B$ records between the two sites, our new data appear to reflect global changes in atmospheric pCO_2, rather than local changes in $[CO_2]_{aq}$. This agreement between sites, despite their contrasting burial depths for the Miocene, also suggests that diagenesis (recrystallisation and/or partial dissolution) is not a major influence on our $\delta^{11}B$ data.

When compared to the benthic foraminiferal $\delta^{18}O$ record these new boron isotope data imply that reduced ice volume and warming during the MCO were associated with high CO_2, and significant ice growth and cooling from 14.7 to 12 Ma were broadly coincident with a CO_2 decline (Fig. 5). It is also clear that the ice-sheet retreats and warming, between 16.5–16 and 15.5–15 Ma, and the first major advance and cooling, between ~14.7 and ~13 Ma, are associated with large and similar magnitude changes in $\delta^{11}B$ (hence also pCO_2). Therefore, because there is little difference between the level of pCO_2 required to melt the continental ice present before and during the MCO, compared to that associated with ice growth during the MMCT, there appears

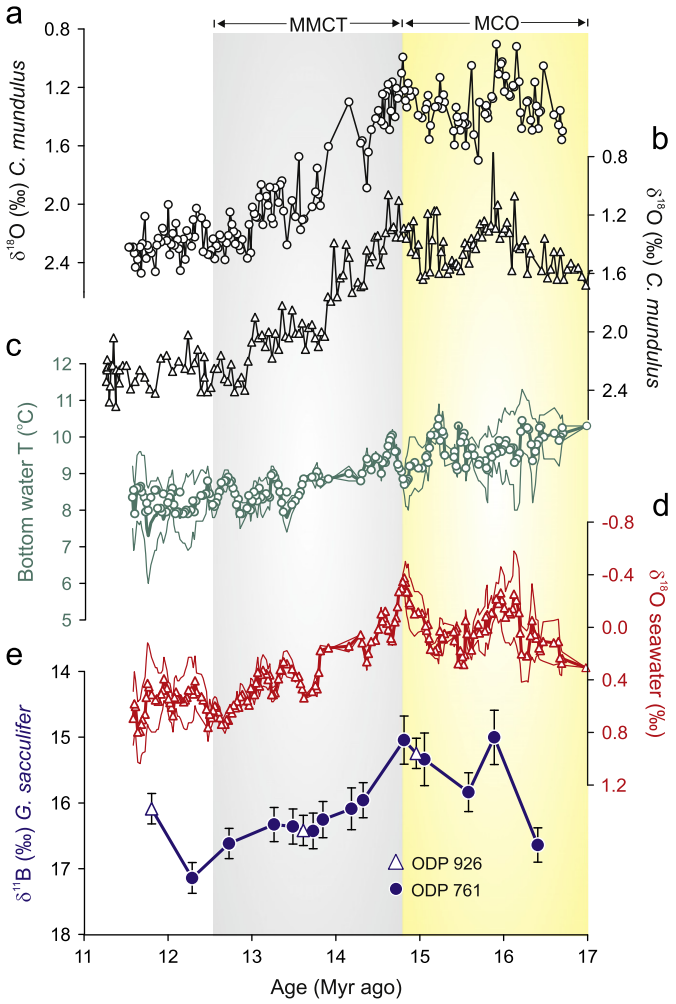

Fig. 5. Boron isotope record ($\delta^{11}B$) compared to $\delta^{18}O$, bottom water temperature and $\delta^{18}O_{sw}$. Benthic foraminiferal (*C. mundulus*) $\delta^{18}O$ from ODP Site 761 (a) from Lear et al. (2010) and (b) from Holbourn et al. (2004). (c) Reconstructed bottom water temperature at ODP Site 761 using Mg/Ca of *Oridorsalis umbonatus* (Lear et al., 2010). (d) Calculated range of $\delta^{18}O$ of seawater (Lear et al., 2010), note the inverted axis and that low $\delta^{18}O_{sw}$ corresponds to low ice volume. (e) $\delta^{11}B$ of *G. sacculifer* (300–355 μm; planktic) from ODP 761 (blue circles) and ODP 926 (blue triangles). Note the inverted axis, with low $\delta^{11}B$ corresponding to low pH and high pCO_2. Error bars show the external reproducibility at 95% confidence. Vertical yellow and grey bars highlight the timing of the middle Miocene Climate Transition (MMCT) and Miocene Climatic Optimum (MCO) as determined by $\delta^{18}O$ at ODP 761. Note that deep water temperature and $\delta^{18}O_{sw}$ are calculated using modern seawater Mg/Ca ratio as in Lear et al. (2010). (For interpretation of the references to colour in this figure legend, the reader is referred to the web version of this article.)

to be no detectable hysteresis between climate forcing by CO_2 and cooling/warming and ice sheet growth/retreat during this time period (Fig. 5).

Benthic $\delta^{18}O$ records are influenced by three parameters: temperature, salinity and global ice volume (e.g. Zachos et al., 2001). The salinity influence is likely to be small in the deep ocean and therefore, at least in theory, an independent thermometer such as Mg/Ca can be used to isolate the oxygen isotope ratio of seawater ($\delta^{18}O_{sw}$) and hence the global ice volume signal (e.g. Lear et al., 2000). Although several estimates of $\delta^{18}O_{sw}$ exist during the Miocene (e.g. Lear et al., 2000; Shevenell et al., 2008), only the study of Lear et al. (2010) directly attempts to account for the influence of $\Delta CO_3^{=}$ on Mg/Ca (Elderfield et al., 2006). The reconstruction of $\delta^{18}O_{sw}$ by Lear et al. (2010), also performed at Site ODP 761 on the same samples analysed here, is shown in Fig. 5. Our new $\delta^{11}B$ record, which largely reflects pCO_2, can therefore be readily compared to estimates of $\delta^{18}O_{sw}$, which largely reflects variation in ice-volume (Fig. 5). Such a comparison indicates that climate (ice-volume) and pCO_2 appear tightly coupled during the MCO and MMCT and that there is no evidence for significant hysteresis or non-linearity in the ice-sheet response to CO_2 forcing. This close correspondence is confirmed by the well-defined linear relationship between $\delta^{11}B_{sac}$ and contemporaneous $\delta^{18}O_{sw}$ (Fig. 6).

3.2. Absolute estimates of pCO_2 change during the middle Miocene

3.2.1. Estimating pCO_2 from $\delta^{11}B_{sac}$

In order to better understand the role of atmospheric CO_2 in determining the evolution of the climate system in the middle Miocene absolute constraints on pCO_2 are required. However, to do this using $\delta^{11}B$ a number of parameters need to be estimated: (i) the boron isotopic composition of seawater ($\delta^{11}B_{sw}$) is needed to translate $\delta^{11}B_{sac}$ into surface water pH; (ii) the sea surface temperature (SST) and sea surface salinity (SSS), which affect the pK_B of boric acid, are needed to estimate the pH and $[CO_2]_{aq}$; and (iii) a second carbonate system parameter is required in order to calculate $[CO_2]_{aq}$ from pH. Of these parameters SST and SSS are of least importance because both have little leverage on the calculated pH and pCO_2 (e.g. ~10 ppm/°C; ~2 ppm/psu). SST can also be directly estimated from tandem Mg/Ca analyses of *G. sacculifer*, a well established proxy for SST (e.g. Anand and Elderfield, 2003), once the changing Mg/Ca of seawater has been taken into account (Horita et al., 2002; Table S1).

The required second carbonate system parameter (in this case we use surface water total alkalinity; ALK) is determined, as discussed above, using a palaeo-pH depth profile approach with new benthic and planktic $\delta^{11}B$ measurements from ODP 761 and existing reconstructions of the calcite compensation depth (Tyrrell and Zeebe, 2004; Sime et al., 2007). In the modern Indian Ocean the CCD is around 1.3 km deeper than the calcite saturation horizon (Bostock et al., 2011). Using a CCD depth of 4.4 km at 12.72 Ma (Sime et al., 2007), therefore allows us to calculate that at 3.1 km the $[CO_3^{=}]_{sat} = [CO_3^{=}]_{observed} = 51$ μmol/kg. The pH of the intermediate depth ocean constrained by the $\delta^{11}B$ of benthic foraminifera from ODP 761 is dependent on $\delta^{11}B_{sw}$. However, for a given $\delta^{11}B_{sw}$, and assuming no intermediate to deep gradient in pH, we are able to constrain deep water TA using pH and $[CO_3^{=}]$ of the deep ocean at 12.72 Ma and, given a surface-deep TA gradient (−100 μmol/kg), the TA of the surface waters (Fig. 7). To account for variations in the strength of the alkalinity pump between the modern and the Miocene, and due to uncertainties in the CCD depth, we ascribe an overall uncertainty of ±200 μmol/kg to this estimate of TA. This uncertainty also accounts for any likely changes of this parameter over the course of the middle Miocene.

We used two methods to generate $\delta^{11}B_{sw}$, as described above. Firstly, we assume that the surface to deep pH profile at the Wombat Plateau is the same in the middle Miocene (at 12.72 Ma) as it is today (0.254 pH units; Key et al., 2004). Such a pH difference is calculated for our measured $\delta^{11}B$ values for *G. sacculifer* (planktic) and an average of *C. mundulus* and *C. wuellerstorfi* (benthic) when $\delta^{11}B_{sw} = 37.6$‰ (Fig. 7b). Taking into account the measurement uncertainty on $\delta^{11}B$ (by far the most significant contribution) we estimate $\delta^{11}B_{sw} = 37.6^{+0.4}_{-0.5}$ ‰.

Secondly, we used the $\delta^{13}C$ difference between our benthic and planktic foraminifera to estimate the likely surface to deep pH difference ($\Delta pH_{surface\text{-}deep}$) at 12.72 Ma. Our planktic–benthic $\delta^{11}B$ difference at 12.72 Ma is 3.48‰ (using an average of the $\delta^{11}B$ for the two benthic species analysed; *C. mundulus* and *C. wuellerstorfi*). The planktic-benthic $\delta^{13}C$ difference at 12.72 Ma is 1.39‰, and a similar difference is seen throughout the middle Miocene at Site 761 (Fig. S2). We use a carbon isotope

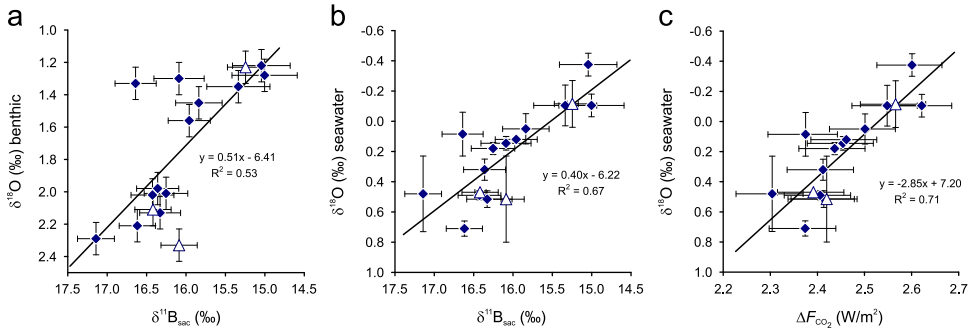

Fig. 6. The relationship between benthic foraminiferal $\delta^{18}O$, $\delta^{18}O_{sw}$ (ice-volume) and climate forcing by pCO_2. (a) The relationship between $\delta^{11}B$ of *G. sacculifer* and contemporaneous $\delta^{18}O$ of benthic foraminifera *C. mundulus* (from Lear et al., 2010). (b) The relationship between $\delta^{11}B$ of *G. sacculifer* and the contemporaneous oxygen isotope composition of seawater ($\delta^{18}O_{sw}$) from Lear et al. (2010). Note the $\delta^{18}O_{sw}$ in Lear et al. (2010) was reconstructed using modern Mg/Ca_{sw} so only relative variation in $\delta^{18}O_{sw}$ should be considered and the absolute values are unlikely to be accurate. (c) The relationship between climate forcing by CO_2 (ΔF_{CO_2}; as defined in text) and $\delta^{18}O_{sw}$ from Lear et al. (2010). In each plot data from ODP 761 is shown as filled blue diamonds and ODP 926 as open blue triangles. Error bars for $\delta^{11}B$ are the 2 sd analytical uncertainty, for ΔF_{CO_2} the error bars relate to the a sum of the analytical uncertainty in $\delta^{11}B$, the uncertainty in TA and sea surface temperature (see text). Uncertainty in $\delta^{18}O_{sw}$ is related to the two estimates made by Lear et al. (2010; with and without taking into account the effect of $\Delta CO_3^{=}$ on Mg/Ca temperature). (For interpretation of the references to colour in this figure legend, the reader is referred to the web version of this article.)

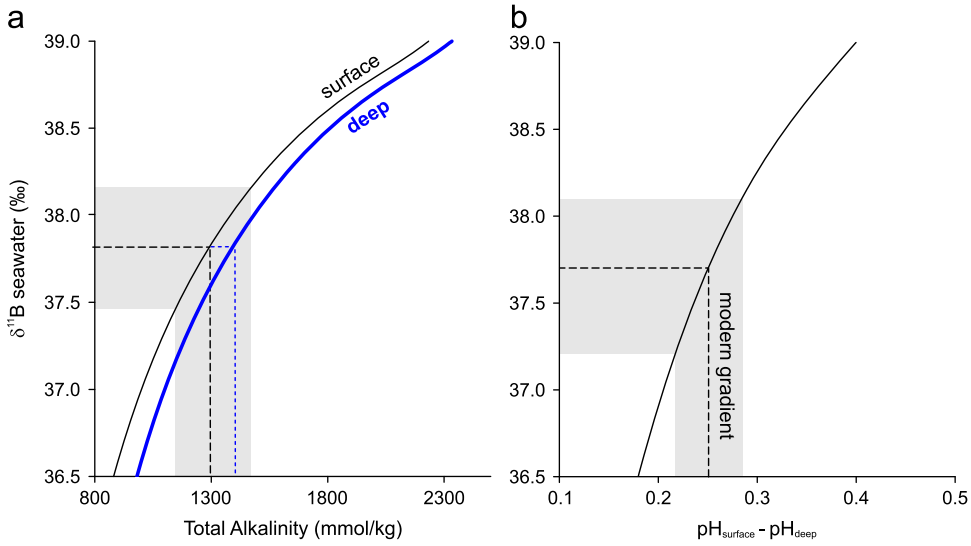

Fig. 7. Variation of surface (black) and deep water (blue) total alkalinity (a; TA) and reconstructed surface to deep pH gradient (b) at 12.72 Ma with varying boron isotopic composition of seawater. The dotted lines and grey bars represent the best estimates and associated uncertainty (see text for details). (For interpretation of the references to colour in this figure legend, the reader is referred to the web version of this article.)

vital effect for *C. mundulus* of +0.47‰ (McCorkle, et al., 1997) and +0.46‰ for *G. sacculifer* (300–355 μm)—an average of that of Spero et al. (2003) and Al-Rousan et al. (2004). Using a pH-$\delta^{13}C_{DIC}$ gradient of 0.201 (Fig. 4), our 1.38‰ $\Delta\delta^{13}C_{DICsurface\text{-}deep}$ equates to a $\Delta pH_{surface\text{-}deep}$ of 0.277 pH units, which is slightly steeper than the modern gradient at the Wombat Plateau of 0.254 pH units. Given our temperature estimates (Table S1) and the palaeo-depth (Holbourn et al., 2004), we require a $\delta^{11}B_{sw}$ of 38.0‰ to generate a $\Delta pH_{surface\text{-}deep}$ of 0.277 pH units from our planktic–benthic $\delta^{11}B$. Uncertainty in the gradient of pH vs. $\delta^{13}C_{DIC}$ is ±0.004 (2 s.e.), which causes an uncertainty of $^{+0.1}_{-0.1}$ ‰ on this estimate of $\delta^{11}B_{sw}$. However, by far the biggest uncertainty in this method is the measurement uncertainty on $\delta^{11}B$ which equates to $^{+0.5}_{-0.6}$ ‰.

A weighted average of both approaches (assuming a symmetrical uncertainty for each estimate for mathematical simplicity and using the "weighted average" function of Isoplot/Ex; Ludwig, 2003) gives a $\delta^{11}B_{sw} = 37.82 \pm 0.35$‰ ($2\sigma$) which we apply for our entire record. Notably, both our estimates are within the published model output (37.4–39.5‰; Lemarchand et al., 2002) and are similar to previous empirical estimates (38.21‰; Pearson and Palmer, 2000) providing confidence in the accuracy of the result. Using this $\delta^{11}B_{sw}$ we calculate $ALK = 1293^{+180}_{-121}$ μmol/kg, as we noted earlier we place a conservative uncertainty on this estimate of ±200 μmol/kg.

3.3. A comparison of $\delta^{11}B$-based pCO_2 to previous estimates of pCO_2 during the middle Miocene

Our new pCO_2 data calculated using the $\delta^{11}B_{sw}$ and ALK detailed above are compared to previously published pCO_2 estimates for the middle Miocene in Fig. 8. The uncertainty in our pCO_2 estimates ranges from around ±35 ppm to ±90 ppm and is determined as the sum of the uncertainty relating to the $\delta^{11}B$ measurement (±25–60 ppm), uncertainty in our estimated ALK (±25–60 ppm) and uncertainty in sea surface temperature (±10 ppm). In Fig. 8 the influence of varying $\delta^{11}B_{sw}$ by ±0.35‰ is shown. Importantly this does not change our reconstructed pCO_2 significantly beyond the summed uncertainty (typically <75 ppm).

Relatively large differences are seen between our new data measured by MC-ICPMS and earlier boron isotope data collected using NTIMS (Pearson and Palmer, 2000; Fig. 8). This offset is unlikely to be caused by an enhanced diagenetic overprint

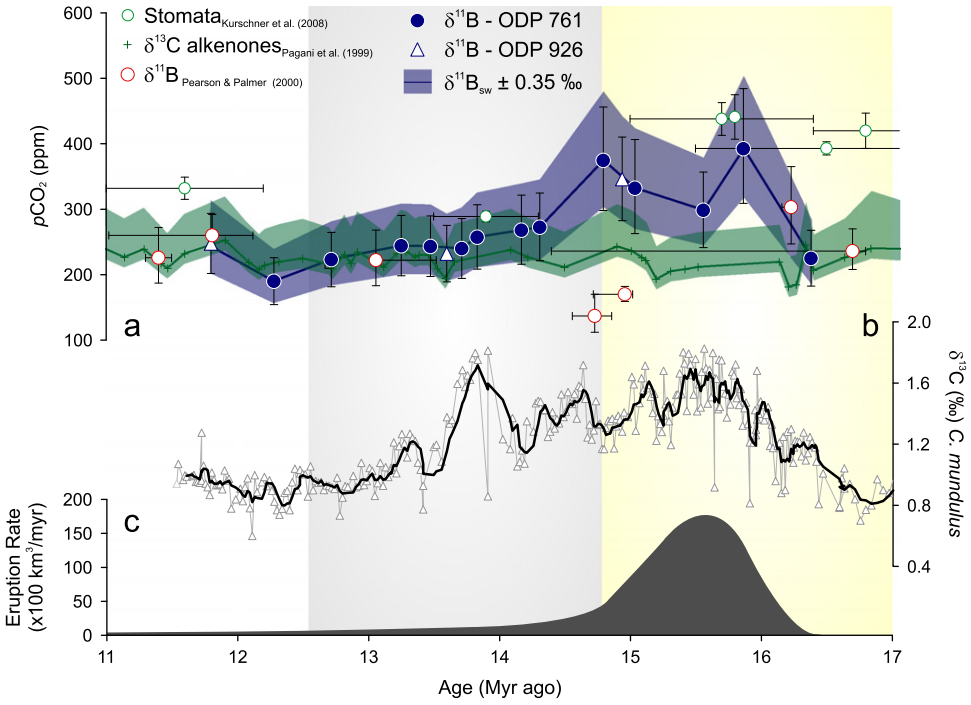

Fig. 8. (a) Comparison of published pCO_2 estimates for the middle Miocene with those of this study (filled blue circles and open blue triangles). Error bars for the $\delta^{11}B$-based pCO_2 from ODP 761 and ODP 926 relate to the combined influence of the uncertainty of the $\delta^{11}B$ measurement, TA estimate and sea surface temperature (see text). The blue band is the uncertainty in pCO_2 related to changing $\delta^{11}B$ of seawater (plus associated change in TA) by $\pm 0.35‰$ (see text). Published boron isotope-based estimates determined using the NTIMS technique are shown as red open circles (Pearson and Palmer, 2000). Open green circles are the pCO_2 estimates based on the density of stomata in fossil leaves (Kürschner et al., 2008) and green crosses (and uncertainty band) are the estimates determined using the $\delta^{13}C$ of sedimentary alkenones (Pagani et al., 1999; green band relating to temperature uncertainty). (b) $\delta^{13}C$ of benthic foraminifera *C. mundulus* from ODP 761 (Lear et al., 2010; Holbourn et al., 2004), the thick black line is a three point running mean. (c) Estimated eruption rate of the Columbia River Flood Basalts from Hooper et al. (2002). Grey and yellow vertical bands show the timing of the middle Miocene climatic optimum (yellow) and Middle Miocene Climate Transition (grey). (For interpretation of the references to colour in this figure legend, the reader is referred to the web version of this article.)

(Schrag, 1999; Pearson et al., 2001) at the ODP Site 871 used in these early studies, given its relatively shallow Miocene burial depth (~75 m). The differences may in part derive from analytical issues (Ni et al., 2010), as significant analytical offsets exist between MC-ICPMS and NTIMS for foraminifera (but not for other carbonates and boric acids; see Foster, 2008; Kasemann et al., 2009; Ni et al., 2010). Also, Pearson and Palmer (2000) used both mixed and single species of foraminifera of several size classes that may have biased their record. A similar variable offset between some NTIMS data (Pearson and Palmer, 2000) and MC-ICPMS was noted for the Mid-Pliocene (Seki et al., 2010). The cause of these differences is the subject of on-going studies, however it is important to note that the accuracy of the new MC-ICPMS technique has been thoroughly documented (Foster, 2008; Ni et al., 2010) and diagenesis is unlikely to significantly influence the data presented here (see above).

On the whole our new boron-isotope based pCO_2 record is similar to the published alkenone record of Pagani et al. (1999) but it differs significantly during the MCO, where the new boron based estimates are up to ~100 ppm higher (Fig. 8). This disagreement is likely due to an underestimate of the sea surface temperatures used in Pagani et al. (1999) as these were based on $\delta^{18}O$ of planktic foraminifera now know to be recrystallised, with potentially erroneous assumptions regarding ice-volume. If sea surface temperatures at the locations used by Pagani et al. (1999) were similar to ODP 761 and ODP 925 then this discrepancy during the MCO is reduced and the estimates overlap within uncertainty.

Similar to previous studies (Seki et al., 2010), and taking into account the relatively large dating uncertainties for terrestrial CO_2 records, we find a very good agreement between our new $\delta^{11}B$ based estimates and those based on the density of stomata in the fossil leaves of extant plant species (Fig. 8; Kürschner et al., 2008). In general this level of agreement with a number of independent techniques is very encouraging and provides confidence in the absolute accuracy of our new $\delta^{11}B$-based pCO_2 record.

3.3.1. *The relationship between pCO_2 and climate in the middle Miocene*

Although our new boron-based Miocene pCO_2 reconstruction is consistent with some previously published studies it clearly exhibits more structure during the middle Miocene (Fig. 8). Specifically we show that pCO_2 reached a maximum value of 392 ± 94 ppm during the MCO and declined to ~200 ppm by ~12 Ma. The temporal coincidence between the period of elevated CO_2 (15–16 Ma) and the main eruptive phase of the Columbia River Flood Basalts (16.1–15 Ma; Hooper et al., 2002; Fig. 8) supports the long-held view that the warmth of the MCO was driven, at least in part, by an increase in volcanic CO_2 emissions (e.g. Hodell and Wodruff, 1994; Kürschner et al., 2008). The subsequent decline in CO_2 during the MMCT may therefore simply have been the result of a cessation of eruption, potentially augmented by enhanced silicate weathering of the fresh flood basalt (e.g. Hodell and Wodruff, 1994; Grard et al., 2005) and increased organic carbon burial (Hodell and Wodruff, 1994), indicated by orbitally paced peaks in the benthic foraminiferal $\delta^{13}C$ (Holbourn et al., 2007) which are broadly coincident with CO_2 drawdown (Fig. 8).

CO_2 exerts a logarithmic forcing on global climate defined by the following relationship (Myhre et al., 1998):

$$\Delta F_{CO_2} = 5.35 \times \mathrm{LN}\left(\frac{C}{C_0}\right) \mathrm{W\,m^{-2}}$$

where C is the CO_2 concentration in ppm and C_0 is the reference pre-industrial concentration (278 ppm). A cross-plot of ΔF_{CO_2} against $\delta^{18}O_{sw}$ for the middle Miocene is well described by a linear relationship ($R^2=0.71$; Fig. 6). Because similar, but not identical (perhaps as could be expected given the importance of other controlling variables), linear relationships also exist for $\delta^{11}B_{sac}$ vs. $\delta^{18}O$ and $\delta^{18}O_{sw}$ (Fig. 6) this relationship is independent of the way in which we calculate pCO_2 and largely independent of how we estimate ice-volume (also compare the broadly similar reconstructions of $\delta^{18}O_{sw}$ by Lear et al. (2010) and Shevenell et al. (2008); Fig. 9). This treatment indicates that within our relatively limited temporal resolution (1 sample per ~300 kyr) and uncertainty (~ ± 50 ppm), pCO_2, climate and ice volume (sea level) are tightly coupled during the middle Miocene and confirms our observation based on $\delta^{11}B$ and $\delta^{18}O_{sw}$ alone that there is no evidence for significant (>300 kyr) hysteresis or non-linearity in the response of ice volume during the MCO and MMCT to climate forcing by CO_2.

Taken at face value, and assuming that the middle Miocene is associated with a relatively dynamic land-based AIS (De Boer et al., 2010), these data suggest that during the middle Miocene at least, the required pCO_2 for the rapid growth and decay of the land-based AIS are similar and much lower than some models suggest (~400 ± 100 ppm vs. ~1000 ppm; Pollard and DeConto,

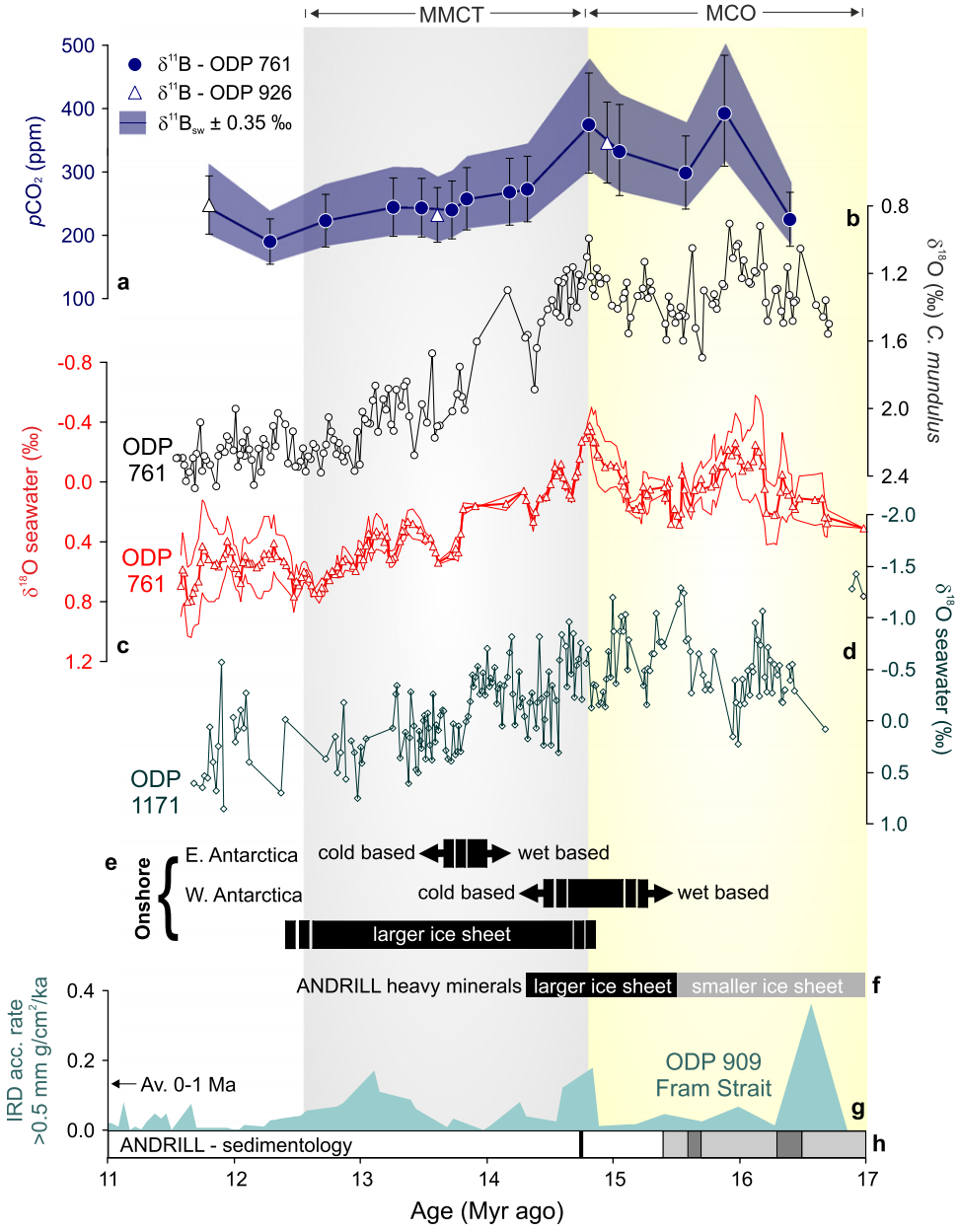

Fig. 9. (a) Middle Miocene pCO_2 (this study), (b) benthic foraminiferal $\delta^{18}O$ at ODP 761 (Lear et al., 2010), (c) $\delta^{18}O$ of seawater ($\delta^{18}O_{sw}$) reconstructed at ODP 761 (Lear et al., 2010), (d) $\delta^{18}O_{sw}$ reconstructed ODP 1171 (Shevenell et al., 2008), (e) schematic summary of shore based reconstructions of the Antarctic Ice Sheet with the length of the black bands incorporating both dating uncertainties and the likely duration of events (Sugden and Denton, 2004; Rocchi et al., 2006; Lewis et al., 2006, 2007, 2008), (f) AIS size based on heavy mineral assemblage in the AND-2A drill hole, Ross Sea (Hauptvogel and Passchier, 2012), (g) accumulation rate of ice rafted debris (IRD) >0.5 mm at ODP 909 from the Fram Strait in the North Atlantic (Winkler et al., 2002) and (h) schematic Antarctic glacial history based on the results from the AND-2A drill hole, Ross Sea (Passchier et al., 2011). For (a) symbols are as for Fig. 8 and for (b) and (c) symbols are as for Fig. 5. Also shown in (g) is the average accumulation rate of IRD >0.5 mm (g/cm^2/ka) at ODP Site 909 during the last 1 million years (0.13 g/cm^2/ka). In (h) the white fill denotes time periods of expanded, cold-based AIS with advance beyond the modern grounding line beginning at ~14.7 Ma (black line) coincident with the start of the MMCT. Periods of polythermal conditions and a reduced AIS compared to the modern are shown as light grey and periods of significant retreat as dark grey (modified from Passchier et al., 2011).

2005). This in turn implies that our understanding of continental-scale ice sheet dynamics and/or the climate system is perhaps flawed, with potentially large implications for the future climate system (e.g. Hansen et al., 2008). One explanation relates to the poor ability of climate models to achieve the relatively high temperatures at high latitudes (i.e. a low equator to polar temperature gradient) that characterise the middle Miocene (Krapp and Jungclaus, 2011) and other warm periods during the Cenozoic (e.g. Huber and Sloan, 2001; Hollis et al., 2009). The simple coupled climate-ice sheet model of Langebroeck et al. (2009) with stronger polar amplification than suggested by modern observations has a lower AIS glaciation threshold at pCO_2 levels of ~400 ppm and a significantly reduced level of hysteresis (deglaciation at ~425 ppm), which is much more consistent with our reconstructions (Figs. 8 and 9).

An alternative explanation involves the observation that pCO_2 values associated with increased ice growth during the MMCT agree well with those thought to be necessary to grow significant land-based ice in the northern hemisphere (~280 ppm; Fig. 9; Seki et al., 2010; DeConto et al., 2008). This, coupled with the lack of significant hysteresis (a feature of the northern hemisphere ice sheets; e.g. Rohling et al., 2009), implies that ice volume and sea level changes during the middle Miocene may not have been caused by a significant advance/retreat of the land-based AIS but instead by the growth and decay of the marine-based western AIS, the Greenland Ice Sheet and some additional land-based ice sheet growth in the northern hemisphere. The modern western AIS and Greenland Ice Sheet can account for up to 14 m (Raymo et al., 2011) of the 55–75 m level fall thought to have occurred during the MMCT (John et al., 2011; Lear et al., 2010). If these estimates of sea level fall are correct, and assuming a minimal contribution of the land-based AIS, 40–60 m of sea level fall at this time would be due to northern hemisphere ice growth. This is equivalent to the sea level fall during marine isotope stage 5b, approximately half of the sea level fall that occurred at the last glacial maximum (LGM; Rohling et al., 2009). Although direct evidence for widespread continental glaciation of the northern hemisphere prior to the Pliocene is limited, a number of high latitude sites that extend to the middle Miocene do exhibit IRD fluxes comparable to that of the Late Pliocene at this time (e.g. Fig. 9; Wolf-Welling et al., 1996; Thiede et al., 1998; Winkler et al., 2002; Krylov et al., 2008), clearly implying some land-based ice in the northern hemisphere during this time period. This requirement of significant northern hemisphere ice growth during the MMCT is reduced to 20–40 m if, as suggested by Pekar and DeConto (2006), AIS volume could increase to up to 125% of today's volume. A larger than modern AIS is also consistent with a larger Antarctic land mass in the past (e.g. Wilson and Luyendyk, 2009), modelling studies for the Plio-Pleistocene (Pollard and DeConto, 2009) and reconstructions which indicate a significantly larger than modern EAIS at the LGM (Peltier, 2004).

Insights into which of these scenarios is correct can be gained from the recent results from the ANDRILL programme and from shore based studies of the relict Miocene landscape on Antarctica. These studies have shown that the AIS was dynamic during the Miocene, undergoing a retreat (but unlikely a full collapse) during the MCO (Passchier et al., 2011; Hauptvogel and Passchier, 2012). What is more, between 15 and 13 Ma, largely coincident with our reconstructed increase in ice volume and drop in pCO_2 (Fig. 5 and 9), these studies indicate a shift from a mobile wet-based to more static cold-based ice sheet that was larger than the modern (Fig. 9; Sugden and Denton, 2004; Lewis et al., 2006, 2007, 2008; Passchier et al., 2011; Hauptvogel and Passchier, 2012). Given the requirement for 55–75 m sea level fall during the MMCT (John et al., 2011), and the likelihood that the AIS did not fully collapse during the MCO, it is most probable that a combination of a more dynamic than modern AIS with some component of northern hemisphere ice was responsible for the variations in ice volume seen during the middle Miocene (Fig. 9). Any part of the land-based AIS involved in the rapid variations in ice volume seen during the middle Miocene must have responded more dynamically to climate forcing at low CO_2 levels than ice-sheet models currently imply (Pollard and DeConto, 2005).

4. Conclusions

Through a combination of planktic $\delta^{11}B$ and benthic $\delta^{18}O$ we have shown that there is a close coupling between pCO_2 and ice-volume (hence climate) through the middle Miocene. The nature of this coupling indicates the presence of a dynamic ice sheet(s) during the MCO and MMCT that, within our sampling resolution (< 300 kyr), exhibited little or no apparent hysteresis and a linear relationship with climate forcing by CO_2. With anthropogenic emissions of CO_2 continuing to rise (and potentially reaching the values we see for the middle Miocene before the middle of this decade), future work must determine whether these waxing and waning Miocene ice sheets were based solely on Antarctica or if some ice growth occurred in the Northern Hemisphere. If ice was completely restricted to Antarctica during the middle Miocene, as some previous studies imply, it would appear that under relatively modest pCO_2 levels close to those existing today, the massive Antarctic ice sheet has the potential to be surprisingly dynamic.

Acknowledgements

This work was supported by NERC grants (NE/D00876X/2, NE/I006176/1 and NE/D008654/1) to G.L.F. and C.H.L. and a NERC studentship to J.W.B.R. We thank the (I)ODP for supplying samples that were essential to this study. Kat Allen and two anonymous reviewers are thanked for their comments that greatly improved this manuscript. Chris Coath and Huw Boulton are acknowledged for their assistance in the laboratory and Paul Wilson, Martin Palmer, Damon Teagle and Eelco Rohling are thanked for their comments on an earlier draft of this manuscript. Are Olsen is also acknowledged for sharing data on the preindustrial $\delta^{13}C_{DIC}$ of the North Atlantic and Amelia Shevenell is thanked for sharing data from ODP 1171.

Appendix A. Supporting information

Supplementary data associated with this article can be found in the online version at http://dx.doi.org/10.1016/j.epsl.2012.06.007.

References

Al-Rousan, S., Patzold, J., Al-Moghrabi, S.M., Wefer, G., 2004. Invasion of anthropogenic CO_2 recorded in planktonic foraminifera from the northern Gulf of Aqaba. Int. J. Earth Sci. 93, 1066–1076.

Alley, R.B., Clark, P.U., Huybrechts, P., Joughin, I., 2005. Ice-sheet and sea-level changes. Science 310, 456–460.

Anand, P., Elderfield, H., 2003. Calibration of Mg/Ca thermometry in planktonic foraminifera from a sediment trap time series. Paleoceanography 18, 1050, doi:1010.1029/2002PA000846.

Barker, S., Greaves, M., Elderfield, H., 2003. A study of cleaning procedures used for foraminiferal Mg/Ca paleothermometry. Geochem. Geophys. Geosyst. 4 (8407), dio:8410,1029/2003GC000559.

Bostock, H.C., Haywood, B.W., Neil, H.L., Currie, K.I., Dunbar, G.B., 2011. Deep-water carbonate concentrations in the southwest Pacific. Deep-Sea Res. I 158, 72–85.

Brown, S.J., Elderfield, H., 1996. Variations in Mg/Ca and Sr/Ca ratios of planktonic foraminifera caused by postdepositional dissolution: evidence of shallow Mg-dependent dissolution. Paleoceanography 11, 543–551.

Catanzaro, E.J., Champion, C.E., Garner, E.L., Marinenko, G., Sappenfield, K.M., Shields, W.R., 1970. Boric assay; isotopic, and assay standard reference materials.

Cooke, P.J., Nelson, C.S., Crundwell, M.P., Spiegler, D., 2002. *Bolboforma* as monitors of Cenozoic palaeoceanographic changes in the Southern Ocean. Palaeogeogr. Palaeoclimatol. Palaeoecol. 188, 73–100.

Coxall, H.K., Wilson, P.A., Palike, H., Lear, C.H., Backman, J., 2005. Rapid stepwise onset of Antarctic glaciation and deeper calcite compensation in the Pacific Ocean. Nature 433, 53–57.

De Boer, B., Van de Wal, R.S.W., Bintanja, R., Lourens, L.J., Tuenter, E., 2010. Cenozoic global ice-volume and temperature simulations with 1-D ice-sheet models forced by benthic $\delta^{18}O$ records. Ann. Glaciol. 51, 23–33.

DeConto, R.M., Pollard, D., Wilson, P.A., Palike, H., Lear, C.H., Pagani, M., 2008. Thresholds for Cenozoic bipolar glaciation. Nature, 455.

Dickson, A., Sabine, C., Christian, J., 2007. Guide to Best Practises for Ocean CO_2 Measurements. North Pacific Marine Science Organization, Sidney, British Columbia.

Dickson, A.G., 1990. Thermodynamics of the dissociation of boric acid in synthetic seawater from 273.15 to 318.15 K. Deep-Sea Res. A. Oceanogr. Res. Pap. 37, 755–766.

Elderfield, H., Yu, J., Anand, P., Kiefer, T., Nyland, B., 2006. Calibrations for benthic foraminiferal Mg/Ca paleothermometry and the carbonate ion hypothesis. Earth Planet. Sci. Lett. 250, 633–649.

Foster, G.L., 2008. Seawater pH, pCO_2 and $[CO_3^{2-}]$ variations in the Caribbean Sea over the last 130 kyr: a boron isotope and B/Ca study of planktic foraminifera. Earth Planet. Sci. Lett. 271, 254–266.

Foster, G.L., Pogge von Strandmann, P.A.E., Rae, J.W.B., 2010. Boron and magnesium isotopic composition of seawater. Geochem. Geophys. Geosyst. 11, Q08015 doi:08010.01029/02010GC003201.

Freeman, K.H., Hayes, J.M., 1992. Fractionation of carbon isotopes by phytoplankton and estimates of ancient CO_2 levels. Global Biogeochem. cycles 6, 185–198.

Grard, A., Francois, L.M., Dessert, C., Dupre, B., Godderis, Y., 2005. Basaltic volcanism and mass extinction at the Permo-Triassic boundary: environmental impact and modeling of the global carbon cycle. Earth Planet. Sci. Lett. 234, 207–221.

Hansen, J.E., Sato, M., Kharecha, P., Beerling, D.J., Berner, R.A., Masson-Delmotte, V., Pagani, M., Royer, D.L., Zachos, J.C., 2008. Target atmospheric CO_2: where should humanity aim? Open Atmos. Sci. J. 2, 217–231.

Hauptvogel, D.W., Passchier, S., 2012. Early–Middle Miocene (17–14 Ma) Antarctic ice dynamics reconstructed from the heavy mineral provenance in the AND-2A drill core, Ross Sea, Antarctica. Global Planet. Change 82-83, 38–50.

Hemming, N.G., Hanson, G.N., 1992. Boron isotopic composition and concentration in modern marine carbonates. Geochim. Cosmochim. Acta 56, 537–543.

Hershey, J.P., Fernadez, M., Milne, P.J., Millero, F.J., 1986. The ionization of boric acid in NaCl, Na–Ca–Cl and Na–Mg–Cl solutions at 25 °C. Geochm. Cosmochim. Acta 50, 143–148.

Hodell, D.A., Wodruff, F., 1994. Variations in the strontium isotopic ratio of seawater during the Miocene: stratigraphic and geochemical implications. Paleoceanography 9, 405–426.

Holbourn, A., Kuhnt, W., Schulz, M., Flores, J.-A., Andersen, N., 2007. Orbitally-paced climate evolution during the middle Miocene "Monterey" carbon-isotope excursion. Earth Planet. Sci. Lett. 261, 534–550.

Holbourn, A., Kuhnt, W., Simo, J.A.T., Li, Q., 2004. Middle Miocene isotope stratigraphy and paleoceanographic evolution of the northwest and southwest Australian margins (Wombat Plateau and Great Australian Bight). Palaeogeogr. Palaeoclim. Palaeoecol. 208, 1–22.

Hollis, C.J., Handley, L., Crouch, E.M., Morgans, H.E.G., Baker, J.A., Creech, J., Collins, K.S., Gibbs, S.J., Huber, M., Schouten, S., Zachos, J., Pancost, R.D., 2009. Tropical sea temperatures in the high-lattitude South Pacific during the Eocene. Geology 37, 99–102.

Hönisch, B., Bijma, J., Russell, A.D., Spero, H.J., Palmer, M.R., Zeebe, R.E., Eisenhauer, A., 2003. The influence of symbiont photosynthesis on the boron isotopic composition of foraminifera shells. Mar. Micropaleontol. 49, 87–96.

Hönisch, B., Hemming, G.N., 2004. Ground-truthing the boron isotope-paleo-pH proxy in planktonic foraminifera shells: partial dissolution and shell size effects. Paleoceanography 19, PA4010, http://dx.doi.org/10.1029/2004PA001026.

Hönisch, B., Hemming, N.G., 2005. Surface ocean pH response to variations in pCO_2 through two full glacial cycles. Earth Planet. Sci. Lett. 236, 305–314.

Hooper, P.R., Binger, G.B., Lees, K.R., 2002. Ages of the Steens and Columbia River flood basalt and their relationship to extension-related calc-alkalic volcanism in eastern Oregon. Geol. Soc. Am. Bull. 114, 43–50.

Horita, J., Zimmermann, H., Holland, H.D., 2002. Chemical evolution of seawater during the Phanerozoic: implications form the record of marine evaporites. Geochim. Cosmochim. Acta 66, 3733–3756.

Huber, M., Sloan, L.C., 2001. Heat transport, deep waters, and thermal gradients: coupled simulation of an Eocene Greenhouse Climate. Geophys. Res. Lett. 28, 3481–3484.

John, C.M., Karner, G.D., Browning, E., Leckie, R.M., Mateo, Z., Carson, B., Lowery, C., 2011. Timing and magnitude of Miocene eustacy derived from the mixed siliciclastic–carbonate startigraphic record of the northeastern Australian margin. Earth Planet. Sci. Lett. 304, 455–467.

Kasemann, S., Schmidt, D.N., Bijma, J., Foster, G.L., 2009. In situ boron isotope analysis of marine carbonates and its application for foraminifera and palaeo-pH. Chem. Geol. 260, 138–147.

Key, R.M., Kozyr, A., Sabine, C.L., Lee, K., Wanninkhof, R., Bullister, J.L., Feely, R.A., Millero, F.J., Mordy, C., Peng, T.-H., 2004. A global ocean carbon climatology: results from Global Data Analysis Project (GLODAP). Global Biogeochem. Cycles 18, GB4031, doi:4010.1029/2004GB002247.

Klochko, K., Cody, G.D., Tossell, J.A., Dera, P., Kaufman, A.J., 2009. Re-evaluating boron speciation in biogenic calcite and aragonite using ^{11}B MAS NMR. Geochim. Cosmochim. Acta 73, 1890–1900.

Klochko, K., Kaufman, A.J., Yoa, W., Byrne, R.H., Tossell, J.A., 2006. Experimental measurement of boron isotope fractionation in seawater. Earth Planet. Sci. Lett. 248, 261–270.

Kominz, M.A., Brown, J.V., Miller, K.G., Sugarman, P.J., Mizintseva, S., Scotese, C.R., 2008. Late Cretaceous to Miocene sea-level estimates from the New Jersey and Delaware coastal plain coreholes: an error analysis. Basin Res. 20, 211–226.

Krapp, M., Jungclaus, J.H., 2011. The Middle Miocene climate as modelled in an atmosphere–ocean–biosphere model. Clim. Past 7, 11–69-1188.

Krylov, A.A., Andreeva, I.A., Vogt, C., Backman, J., Krupskaya, V.V., Grikurov, G.E., Moran, K., Shoji, H., 2008. A shift in heavy and clay mineral provenance indicates a middle Miocene onset of perennial sea ice cover in teh Arctic Ocean. Paleoceanography, 23, http://dx.doi.org/10.1029/2007PA001497.

Kürschner, W.M., Kvacek, Z., Dilcher, D.L., 2008. The impact of Miocene atmospheric carbon dioxide fluctuations on climate and the evolution of terrestrial ecosystems. Proc. Natl. Acad. Sci. 105, 440–453.

Langebroeck, P.M., Paul, A., Schulz, M., 2009. Antarctic ice-sheet response to atmospheric CO_2 and insolation in the Middle Miocene. Clim. Past 5, 633–646.

Lear, C.H., Elderfield, H., Wilson, P.A., 2000. Cenozoic deep-sea temperatures and global ice volumes from Mg/Ca in benthic foraminiferal calcite. Science 287, 269–272.

Lear, C.H., Mawbey, E.M., Rosenthal, Y., 2010. Cenozoic benthic foraminiferal Mg/Ca and Li/Ca records: toward unlocking temperatures and saturation states. Paleoceanography http://dx.doi.org/10.1029/2009PA001880.

Lear, C.H., Rosenthal, Y., Slowey, N., 2002. Benthic foraminiferal Mg/Ca-paleothermomentry: a revised core-top calibration. Geochim. Cosmochim. Acta 66, 3375–3387.

Lee, K., Kim, T.-W., Byrne, R.H., Millero, F.J., Feely, R.A., Liu, Y.-M., 2010. The universal ratio of boron to chlorinity for the North Pacific and North Atlantic oceans. Geochim. Cosmochim. Acta 74, 1801–1811.

Lemarchand, D., Gaillardet, J., Lewin, E., Allegre, C.J., 2002. Boron isotope systematics in large rivers: implications for the marine boron budget and paleo-pH reconstruction over the Cenozoic. Chem. Geol. 190, 123–140.

Lewis, A.R., Marchant, D.R., Ashworth, A.C., Hedenas, L., Hemming, S.R., Johnson, J.V., Leng, M.J., Machlus, M.L., Newton, A.E., Raine, J.I., Willenbring, J.K., Williams, M., Wolfe, A.P., 2008. Mid-Miocene cooling and the extinction of tundra in continental Antarctica. Proc. Natl. Acad. Sci. 105, 10676–10680.

Lewis, A.R., Marchant, D.R., Ashworth, A.C., Hemming, S.R., Machlus, M.L., 2007. Major middle Miocene global climate change: evidence from East Antarctica and the Transantarctic Mountains. Geol. Soc. Am. Bull. 119, 1449–1461.

Lewis, A.R., Marchant, D.R., Kowalewski, D.E., Baldwin, S.L., Webb, L.E., 2006. The age and origin of the Labyrinth, western Dry Valleys, Antarctica: evidence for extensive middle Miocene subglacial floods and freshwater discharge to the Southern Ocean. Geology 34, 513–516.

Liebrand, D., Lourens, L.J., Hodell, D.A., de Boer, B., van de Wal, R.S.W., Palike, H., 2011. Antarctic ice sheet and oceanogrpahic response to eccentricity forcing during early Miocene. Clim. Past 7, 869–880.

Ludwig, K.R., 2003. User's Manual for Isoplot/Ex, Version 3.0, A Geochronological Toolkit for Microsoft Excel, Berkeley Geochronology Center Special Publication No. 4.

Lyle, M., 2003. Neogene carbonate burial in the Pacific Ocean. Paleoceanography 18 1959, doi:1910.1029/2002PA000777.

Lynch-Stieglitz, J., Stocker, T.F., Broecker, W.S., Fairbanks, R.G., 1995. The influence of air–sea exchange on the isotopic composition of oceanic carbon—observations and modelling. Global Biogeochem. cycles 9, 653–665.

Mudelsee, M., Raymo, M.E., 2005. Slow dynamics of the Northern Hemisphere glaciation. Paleoceanography, 20, http://dx.doi.org/10.1029/2005PA001153.

Myhre, G., Highwood, E.J., Shine, K.P., Stordal, F., 1998. New estimates of radiative forcing due to well mixed greenhouse gases. Geophys. Res. Lett. 25, 2715–2718.

Ni, Y., Foster, G.L., Bailey, T., Elliott, T., Schmidt, D.N., Pearson, P., Haley, B., Coath, C.D., 2007. A core top assessment of proxies for the ocean carbonate system in surface-dwelling foraminifers. Paleoceanography, 22, http://dx.doi.org/10.1029/2006PA001337.

Ni, Y., Foster, G.L., Elliott, T., 2010. The accuracy of $\delta^{11}B$ measurements of foraminifers. Chem. Geol. 274, 187–195.

Olsen, A., Ninneman, U.S., 2010. Large $\delta^{13}C$ gradients in the preindustrial North Atlantic revealed. Science 330, 658–659.

Pagani, M., Freeman, K.H., Arthur, M.A., 1999. Late Miocene atmospheric CO_2 concentrations and the expansion of C_4 grasses. Science 285, 876–879.

Paris, G., Gaillardet, J., Louvat, P., 2010. Geological evolution of seawater boron isotopic composition recorded in evaporites. Geology 38, 1035–1038.

Passchier, S., Browne, G., Field, B., Fielding, C.R., Krissek, L.A., Panter, K.S., Pekar, S.F., Team, A.-S.S., 2011. Early and middle Miocene Antarctic glacial history from the sedimentary facies distribution in the AND-2A drill hole, Ross Sea, Antarctica. Geol. Soc. Am. Bull. 123, 2352–2365.

Pearson, P.N., Ditchfield, P.W., Singano, J., Harcourt-Brown, K.G., Nicholas, C.J., Olsson, R.K., Shackleton, N.J., Hall, M.A., 2001. Warm tropical sea surface temperatures in the Late Cretaceous and Eocene epochs. Nature 413, 481–487.

Pearson, P.N., Palmer, M.R., 2000. Atmospheric carbon dioxide concentrations over the past 60 million years. Nature 406, 695–699.

Pekar, S.F., deConto, R.M., 2006. High-resolution ice-volume estimates for the early Miocene: evidence for a dynamic ice sheet in Antarctica. Palaeogeogr. Palaeoclimatol. Palaeoecol. 231, 101–109.
Peltier, W.R., 2004. Global glacial isostasy and the surface of the ice-age Earth: the ICE-5G (VM2) Model and GRACE. Ann. Rev. Earth Planet. Sci. 32, 111–149.
Pollard, D., DeConto, R.M., 2005. Hysteresis in Cenozoic Antarctic ice-sheet variations. Global Planet. Change 45, 9–21.
Pollard, D., DeConto, R.M., 2009. Modelling West Antarctic ice sheet growth and collapse through the past five million years. Nature 458, 329–332.
Rae, J.W.B., Foster, G.L., Schmidt, D.N., Elliott, T., 2011. Boron isotopes and B/Ca in benthic foraminifera: proxies for the deep ocean carbonate system. Earth Planet. Sci. Lett. 302, 403–413.
Rahmstorf, S., Cazenave, A., Church, J.A., Hansen, J.E., Keeling, R.F., Parker, D.E., Somerville, R.C.J., 2007. Recent climate observations compared to projections. Science 316, 709.
Raymo, M.E., Mitrovica, J.X., O'Leary, M.J., DeConto, R.M., HEarty, P.J., 2011. Departures from eustacy in Pliocene sea-level records. Nat. Geosci. 4, 328–332.
Rocchi, S., Le Masurier, W.E., Di Vincenzo, G., 2006. Oligocene to Holocene erosion and glacial history in Marie Byrd Land, West Antarctica, inferred from exhumation of the Dorrel Rock intrustive complex and from volcano morphologies. Geol. Soc. Am. Bull. 118, 991–1005.
Rohling, E.J., Grant, K., Bolshaw, M., Roberts, A.P., Siddall, M., Hemleben, C., Kucera, M., 2009. Antarctic temperature and global sea level closely coupled over the past five glacial cycles. Nat. Geosci. 2, 500–504.
Rollion-Bard, C., Blamart, D., Trebosc, J., Tricot, G., Mussi, A., Cuif, J.-P., 2011. Boron isotopes as pH proxy: a new look at boron speciation in deep-sea corals using ^{11}B MAS NMR and EELS. Geochim. Cosmochim. Acta 75, 1003–1012.
Sanyal, A., Bijma, J., Spero, H.J., Lea, D., 2001. Empirical relationship between pH and the boroan isotopic composition of *Globigerinoides sacculifer*: implications for the boron isotope paleo-pH proxy. Paleoceanography 16, 515–519.
Sanyal, A., Hemming, N.G., Hanson, G.N., Broecker, W.S., 1995. Evidence for a higher pH in the glacial ocean from boron isotopes in foraminifera. Nature 373, 234–236.
Schrag, D.P., 1999. Effects of diagenesis on the isotopic record of late Paleogene tropical sea surface temperatures. Chem. Geol. 161, 215–244.
Seki, O., Foster, G.L., Schmidt, D.N., Mackensen, A., Kawamura, K., Pancost, R.D., 2010. Alkenone and boron based Plio-Pleistocene pCO_2 records. Earth Planet. Sci. Lett. 292, 201–211.
Shevenell, A.E., Kennett, J.P., Lea, D.W., 2008. Middle Miocene ice sheet dynamics, deep-sea temperatures, and carbon cycling: a Southern Ocean perspective. Geochem. Geophys. Geosyst. 9, Q02006, doi:02010.01029/02007GC001736.
Sime, N.G., de La Rocha, C.L., Tipper, E.T., Tripati, A., Galy, A., Bickle, M.J., 2007. Interpreting the Ca isotope record of marine biogenic carbonates. Geochim. Cosmochim. Acta 71, 3979–3989.
Simon, L., Lecuyer, C., Marechal, C., Coltice, N., 2006. Modelling the geochemical cycle of boron: implications for the long-term δ^{11}B evolution of seawater and oceanic crust. Chem. Geol. 225, 61–76.
Spero, H.J., Mielke, E.M., Lea, D.W., Pak, D.K., 2003. Multispecies approach to reconstructing eastern equatorial Pacific thermocline hydography during the past 360 kyr. Paleoceanography 18, 1022, doi:1010.1029/2002PA000814.
Sugden, D., Denton, G., 2004. Cenozoic landscape evolution of the Convoy Range to Mackay Glacier area, Transantarctic Mountains: onshore to offshore synthesis. Geol. Soc. Am. Bull. 116, 840–857.
Takahashi, K., Sutherland, S.C., Wanninkhof, R., Sweeney, C., Feely, R.A., Chipman, D.W., Hales, B., Friederich, G., Chavez, F., Sabine, C., Watson, A., Bakker, D.C.E., Schuster, U., Metzl, N., Yoshikawa-Inoue, H., Ishii, M., Midorikawa, T., Nojiri, Y., Kortzinger, A., Steinhoff, T., Hoppema, M., Olafsson, J., Arnarson, T.S., Tilbrook, B., Johannessen, T., Olsen, A., Bellerby, R., Wong, C.S., Delille, B., Bates, N.R., de Baar, H.J.W., 2009. Climatological mean and decadal change in surface ocean pCO_2, and net sea–air CO_2 flux over the global oceans. Deep-Sea Res. II 56, 554–577.
Thiede, J., Winkler, A., Wolf-Welling, T., Eldholm, O., Myhre, A., Baumann, K.-H., Heinrich, R., Stein, R., 1998. Late Cenozoic history of the polar North Atlantic: results from ocean drilling. Quat. Sci. Rev. 17, 185–208.
Tyrrell, T., Zeebe, R.E., 2004. History of carbonate ion concentration over the last 100 million years. Geochim. Cosmochim. Acta 68, 3521–3530.
Wilson, D.S., Luyendyk, B.P., 2009. West Antarctic paleotopography estimated at the Eocene–Oligocene climate transistion. Geophys. Res. Lett. 36, L16302, http://dx.doi.org/10.1029/2009GL039297.
Winkler, A., Wolf-Welling, T.C.W., Stattegger, K., Thiede, J., 2002. Clay mineral sedimentation in high northern latitude deep-sea basins since the Middle Miocene (ODP Leg 151, NAAG). Int. J. Earth Sci. 91, 133–148.
Woodruff, F., Savin, S.M., 1991. Mid-Miocene isotope stratigraphy in the deep sea: high-resolution correlations, paleoclimate cycles, and sediment preservation. Paleoceanography 6, 755–806.
Wolf-Welling, T.C.W., Cremer, M., O'Connell, S., Winkler, A., Thiede, J., 1996. Cenozoic arctic gateway paleoclimate variability: indications from changes in coarse-fraction composition, in: Thiede, J., Myhre, A.M., Firth, J.V., Johnson, G.L., Ruddiman, W.F. (Eds.), Proceedings of the Ocean Drilling Program, Scientific Results. Ocean Drilling Program, College Station, Texas, pp. 515–567.
You, Y., Huber, M., Muller, R.D., Poulsen, C.J., Ribbe, J., 2009. Simulation of the Middle Miocene climatic optimum. Geophys. Res. Lett., 36, http://dx.doi.org/10.1029/2008GL036571.
Yu, J., Elderfield, H., Greaves, M., Day, J., 2007. Preferential dissolution of benthic foraminiferal calcite during laboratory reductive cleaning. Geochem. Geophys. Geosyst., Q06016, http://dx.doi.org/10.1029/2006GC001571.
Zachos, J.C., Pagani, M., Sloan, L., Thomas, E., Billups, K., 2001. Trends, rhythms, and aberrations in global climate 65 Ma to present. Science 292, 686–693.
Zeebe, R.E., Wolf-Gladrow, D.A., Bijma, J., Honisch, B., 2003. Vital effects in foraminifera do not compromise the use of δ^{11}B as a paleo-pH indicator: evidence from modeling. Paleoceanography 18, 1043, http://dx.doi.org/10.1029/2003PA000881.